


Cite this: *RSC Adv.*, 2025, 15, 3378

# Developing a highly sensitive electrochemical sensor for malathion detection based on green g-C<sub>3</sub>N<sub>4</sub>@LiCoO<sub>2</sub> nanocomposites

Nafis Ahmad,<sup>\*a</sup> Anjan Kumar,<sup>b</sup> Nikunj Rachchh,<sup>c</sup> Renuka Jyothi S,<sup>d</sup> Deepak Bhanot,<sup>e</sup> Bharti Kumari,<sup>f</sup> Abhinav Kumar<sup>g</sup> and Munthar Kadhim Abosaoda<sup>h</sup>

Nowadays, developing pesticide-free agriculture is highly demanded by society. The development of electrochemical sensors to monitor and control pesticides is an effective step toward this desired goal. The current research has faced this issue by modifying of glassy carbon electrodes (GCEs) with green g-C<sub>3</sub>N<sub>4</sub>@LiCoO<sub>2</sub> nanocomposites to probe malathion, an organophosphate pesticide. The g-C<sub>3</sub>N<sub>4</sub>@LiCoO<sub>2</sub> modified GCE showed higher current than the net GCE, as a result of improved electrocatalytic performance of the modified GCE to oxidize malathion. Increased malathion concentration enhanced the malathion oxidation anodic peak current at +410 mV caused by the g-C<sub>3</sub>N<sub>4</sub>@LiCoO<sub>2</sub> modified GCE. The developed probe showed an excellent linear response for malathion detection in the 5–120 nM ( $R^2 = 0.994$ ) range and recorded a limit of detection of 4.38 nM. Besides, the modified GCE reveals considerable stability and reproducibility, which offers a cost-effective, sensitive, and selective electrode for malathion probing.

Received 11th November 2024

Accepted 28th January 2025

DOI: 10.1039/d4ra08023h

rsc.li/rsc-advances

## 1. Introduction

Organic pesticides (OPs) such as organophosphorus are commonly used to safeguard crops from pests.<sup>1,2</sup> These potent molecules pose a significant risk to humans and animals, as they can be absorbed by living organisms through various harmful pathways. Another group of harmful organic compounds is organochlorine insecticides, which can have devastating effects on all life forms, leading to environmental degradation and ecosystem pollution. Malathion, in particular,

when used in large quantities, can be extremely harmful, impacting aquatic organisms, vertebrates, and humans by disrupting neurological functions, causing adverse effects such as headaches and nausea, and significantly compromising immune systems. Not only does it pose a threat to living beings, but it also contaminates agricultural produce and groundwater. Consequently, detecting OPs requires a precise, rapid, sensitive, and dependable analytical approach.<sup>2–5</sup> Lately, individuals have innovated various detection techniques like GC,<sup>6</sup> HPLC,<sup>7</sup> MS,<sup>8</sup> and ECL.<sup>9,10</sup> Of these, ECL sensors have garnered significant interest because of their straightforward usability, heightened sensitivity, and cost-effectiveness. This method excels in swift detection processes. A chemical sensor, as per the IUPAC<sup>11</sup> definition, is a tool that transforms chemical information, spanning from the levels of an individual substance in a sample to a comprehensive analysis of its composition, into a signal suitable for analysis. Primarily, a chemical sensor comprises two key components: a receptor and a physicochemical transducer. Receptors exhibit variability and can include activated or doped surfaces and intricate (macro) molecules that establish highly precise connections with the substance being analyzed. Catalytic sensors leverage catalytic processes to produce the signal.<sup>12</sup> As the dominant players in the market, electrochemical sensors are widely used primarily because of their benefits, such as their ability to achieve low detection limits, sometimes as minute as picomoles.<sup>13</sup> The increasing need for trace pesticide detection methods that are quick, precise, sensitive, easy to use, and durable compared to traditional methods is evident.<sup>14–18</sup>

<sup>a</sup>Department of Physics, College of Science, King Khalid University, Abha 61413, Saudi Arabia. E-mail: nafis.jmi@gmail.com

<sup>b</sup>Department of Electronics and Communication Engineering, GLA University, Mathura-281406, India

<sup>c</sup>Marwadi University Research Center, Department of Mechanical Engineering, Faculty of Engineering & Technology, Marwadi University, Rajkot-360003, Gujarat, India

<sup>d</sup>Department of Biotechnology and Genetics, School of Sciences, JAIN (Deemed to be University), Bangalore, Karnataka, India

<sup>e</sup>Centre for Research Impact & Outcome, Chitkara University Institute of Engineering and Technology, Chitkara University, Rajpura, 140401, Punjab, India

<sup>f</sup>NIMS School of Petroleum & Chemical Engineering, NIMS University Rajasthan, Jaipur, India

<sup>g</sup>Department of Nuclear and Renewable Energy, Ural Federal University Named after the First President of Russia Boris Yeltsin, Ekaterinburg 620002, Russia

<sup>h</sup>College of Pharmacy, The Islamic University, Najaf, Iraq. E-mail: munthar.abosaoda@outlook.com

<sup>i</sup>College of Pharmacy, The Islamic University of Al Diwaniyah, Al Diwaniyah, Iraq

<sup>j</sup>Department of Mechanical Engineering, Karpagam Academy of Higher Education, Coimbatore, 641021, India



This demand has been somewhat met by employing various strategies, including non-enzymatic electrochemical detection, a fairly efficient and promising platform for sensing pesticides.<sup>19,20</sup> The utilization of new and sophisticated sensor materials in agricultural settings is currently in its initial phases of advancement compared to other fields.<sup>21–25</sup> Through the progress of sensors and diagnostic tools for on-site monitoring, farmers will be able to observe environmental factors crucial for plant growth and protection closely. By detecting issues early, these monitoring systems can improve productivity while minimizing the need for agricultural chemicals.<sup>26,27</sup> Recent breakthroughs in innovative functional materials include metal-free substances like RGO and  $g-C_3N_4$ .<sup>28–31</sup> Graphitic carbon nitride ( $g-C_3N_4$ ), a metal-free semiconductor, is recognized for its composition—a graphitic  $\pi$ -conjugated layered structure substituted with nitrogen. This structure comprises aromatic heptazine units linked by tertiary amines.<sup>32,33</sup> Due to its unique optical, electronic, and physicochemical properties,  $g-C_3N_4$  has become a desirable candidate for a variety of applications such as solar water splitting, degradation of pollutants using visible-light photocatalysis, optoelectronics, SERS sensing, and bioimaging.<sup>33–38</sup> Nevertheless, the constrained conductivity and significant contact resistance of  $g-C_3N_4$  impede its effectiveness in electrocatalysis, limiting its use in electrochemical fields.

The inherent structure of  $g-C_3N_4$  includes numerous consistent nitrogen centers that can function as active catalyst sites in electrocatalysis. This implies that modifying  $g-C_3N_4$  appropriately could significantly enhance its electrocatalytic performance. Structural modification can involve various methods, such as doping, composite formation, and nanostructuring. Among these methods, creating  $g-C_3N_4$  composites with different materials possessing superior electronic and electrochemical properties, like metal nanoparticles, metal oxides, and semiconductors, is a promising strategy to enhance the electrocatalytic properties of  $g-C_3N_4$ . In sensor exploration, creating an electrochemical sensor that exhibits enhanced selectivity, sensitivity, reproducibility, stability, and detection limit for specific pollutants remains challenging. In this study, we address the critical need for sensitive and reliable malathion detection by developing an electrochemical probe based on green  $g-C_3N_4@LiCoO_2$  nanocomposites. Our approach leverages the synergistic properties of  $g-C_3N_4$  and  $LiCoO_2$  to create a composite material with enhanced electrocatalytic performance. The  $g-C_3N_4@LiCoO_2$  modified GCE demonstrated significantly improved electrocatalytic performance for malathion oxidation compared to bare GCE. The optimized sensor exhibited a linear response for malathion detection in the range of 5–120 nM with a low detection limit of 4.38 nM. Electrochemical studies revealed that incorporating  $LiCoO_2$  into  $g-C_3N_4$  enhanced electron transfer kinetics and increased the electroactive surface area, improving sensitivity, selectivity, and stability. This work contributes to the advancement of pesticide-sensing technology and aligns with the growing demand for sustainable agricultural practices. Our innovative sensor design shows great potential for practical applications in environmental monitoring and food safety, representing a significant

step towards developing efficient, cost-effective, and green solutions for pesticide detection. Ultimately, this research supports the transition to pesticide-free agriculture while promoting public health and environmental protection.

## 2. Experimental

### 2.1 Green synthesis of $LiCoO_2$ nanoparticles

$LiCoO_2$  nanoparticles (NPs) were synthesized through a green process that utilized *Aloe vera* plant extract as a capping agent. 40 g of cleaned *Aloe vera* leaves were finely cut to extract their gel. The obtained gel was diluted with 100 mL of deionized water (DI) *via* sonication for 30 minutes, followed by stirring at 60 °C for two hours. Then, two mmol of each cobalt acetate and lithium acetate were dissolved in 15 mL of DI while stirring for 45 minutes at 60 °C. The obtained solution was mixed with *Aloe vera* extraction solution, followed by refluxing at 70 °C for 24 hours. The refluxed solution was poured into a beaker and heated at 90 °C until a purple paste was obtained. The resultant paste was spread in a ceramic crucible and baked at 750 °C for three hours.

### 2.2 Synthesis of $g-C_3N_4$ nanosheets

15 g melamine (Sigma Aldrich, 99%) was added into 40 mL ethanol (Merck, 99.5%), followed by sonication for 30 minutes at room temperature (RT). Then 500 mg of ammonium sulfate (Merck, 99.5%) was added to the melamine solution and stirred at RT for four hours. After drying the mixed solution in an oven for 12 hours at 50 °C, it was transferred into a ceramic crucible and heated to 500 °C with a 5 °C min<sup>−1</sup> ramp under an inert ambient, then raising the temperature to 550 °C and keeping for two hours at 550 °C. The cooled product was ground to obtain  $g-C_3N_4$  nanosheets.

### 2.3 Preparation $g-C_3N_4@LiCoO_2$ nanocomposite

In four individual vials, 600 mg  $g-C_3N_4$  material was dispersed into 200 mL DI *via* sonication at RT for two hours. In each vial, different weight ratios of 0.4, 0.8, 1.6, and 3.2% of  $LiCoO_2$  NPs, respectively, were added to them, followed by stirring at RT for two hours. The obtained suspensions were separately poured into a Teflon-lined autoclave and baked at 140 °C for six hours. The  $g-C_3N_4@LiCoO_2$  nanostructures were washed with DI and ethanol *via* vacuum filtration. The pre-washed solids were dried in an oven at 80 °C overnight. The prepared  $g-C_3N_4@LiCoO_2$  nanostructures based on 0.4, 0.8, 1.2, and 3.2% of  $LiCoO_2$  NPs are labeled with GL1, GL2, GL3, and GL4, respectively.

### 2.4 Electrode preparation

Polished and washed glassy carbon electrodes (GCEs) with a diameter of 3 mm were coated with prepared materials in this study ( $g-C_3N_4$ ,  $LiCoO_2$ , GL1, GL2, GL3, and GL4). For this aim, 5 mg of the synthesized materials were dispersed in 3 mL of ethanol by sonication for 45 min at RT. Next, 6  $\mu$ L of the above suspensions were dropped cast on net GCEs and dried at RT overnight to form modified GCEs. Then, to conduct the electrochemical tests, including CV, EIS, and DPSV, a three-



electrode cell was employed, in which a platinum electrode, Ag/AgCl electrode, and net GCE or modified GCE were used as a counter, reference, and working electrodes, respectively.

## 2.5 Materials characterization

Electrochemical investigations were conducted on a CHI760E workstation potentiostat. Philips X'PERT diffractometer recorded X-ray diffraction (XRD) patterns of samples. Solid morphologies and energy-dispersive X-ray spectroscopy (EDS) of samples were investigated using TESCAN MIRA3 FESEM equipment. JEOL JEM-2100 TEM microscope was used to further investigation on morphologies of materials. The SAM 800 X-ray photoelectron spectrometer collected XPS spectra of samples. Gemini 2360, Micromeritics Instruments Corp system conducted nitrogen adsorption-desorption analyses to investigate the specific surface area and pore diameter of samples.

## 3. Results

Fig. 1 shows a detailed diagram of the synthesis process for  $g\text{-C}_3\text{N}_4\text{@LiCoO}_2$  nanocomposites, illustrating various steps, including mixing, heating, refluxing, and baking at different temperatures and durations.

The phase formation of all synthesized specimens was confirmed using X-ray diffraction (XRD) analysis (Fig. 2a). The broad diffraction peaks at  $12.74^\circ$  and  $27.32^\circ$  in Fig. 2a(i) correspond to the (100) and (002) planes of  $g\text{-C}_3\text{N}_4$  sheets, respectively.<sup>39,40</sup> All diffraction peaks in Fig. 2a(ii) are indexed to  $\text{LiCoO}_2$ , indicating a typical  $\alpha\text{-NaFeO}_2$  structure with space group  $R\bar{3}m$ .<sup>41,42</sup> The XRD patterns of the GL1, GL2, GL3, and GL4 composites (Fig. 2a(iii)–(vi)) show diffraction peaks associated with both  $\text{LiCoO}_2$  and  $g\text{-C}_3\text{N}_4$ , confirming the successful synthesis of these composites. The Raman spectra of the synthesized  $g\text{-C}_3\text{N}_4$  nanosheets (Fig. 2b) exhibit characteristic peaks that align well with those reported in the literature.<sup>43</sup> The distinct  $E_g$  and  $A_{1g}$  vibrational modes at 488 and  $598\text{ cm}^{-1}$ , respectively, in the  $\text{LiCoO}_2$  Raman spectrum (Fig. 2b(ii)) are assigned to the asymmetric bending mode of O–Co–O and the

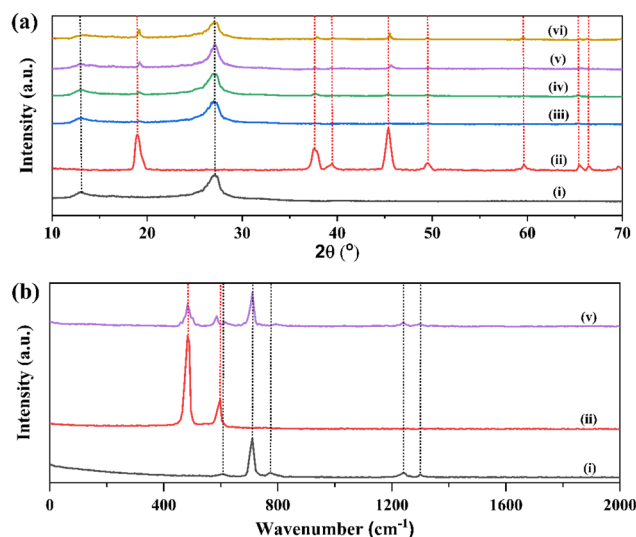


Fig. 2 (a) XRD pattern and (b) Raman spectra of different samples. (i)  $g\text{-C}_3\text{N}_4$ , (ii)  $\text{LiCoO}_2$ , (iii) GL1, (iv) GL2, (v) GL3, and (vi) GL3.

symmetric stretching mode of Co–O.<sup>44</sup> The Raman spectrum of  $\text{GL}_3$  (Fig. 2b(v)) indicates that adding  $g\text{-C}_3\text{N}_4$  does not significantly alter the crystalline structure or purity of  $\text{LiCoO}_2$ , consistent with the XRD results. The shift of the peak at approximately  $598\text{ cm}^{-1}$  in the Raman spectrum indicates a change in the Co–O bond vibration, suggesting due to the interaction with  $g\text{-C}_3\text{N}_4$ .

The  $g\text{-C}_3\text{N}_4$  nanoplates FESEM image reveals a sheet-like morphology, confirming the nanoplate structure of the synthesized  $g\text{-C}_3\text{N}_4$  (Fig. 3a). The  $\text{LiCoO}_2$  nanoparticles FESEM image shows a collection of spherical particles (Fig. 3b). The  $g\text{-C}_3\text{N}_4\text{@LiCoO}_2$  nanocomposites FESEM image demonstrates the successful formation of the hybrid material. The  $\text{LiCoO}_2$  nanoparticles are observed to be well-dispersed and intimately anchored on the  $g\text{-C}_3\text{N}_4$  nanosheets, suggesting a promising composite structure (Fig. 4c). The EDX pattern of the  $g\text{-C}_3\text{N}_4\text{@LiCoO}_2$  nanocomposite is shown in Fig. 3d. The spectrum

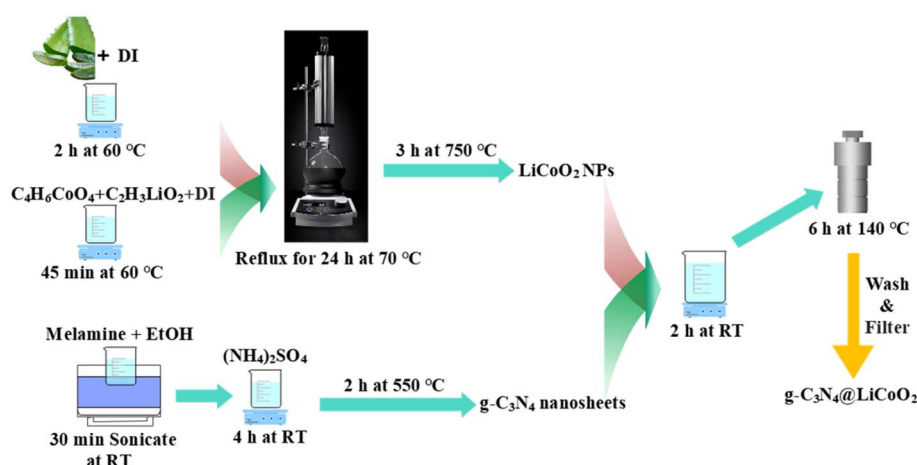


Fig. 1 Schematic view of synthesis process for  $g\text{-C}_3\text{N}_4\text{@LiCoO}_2$  nanocomposites.

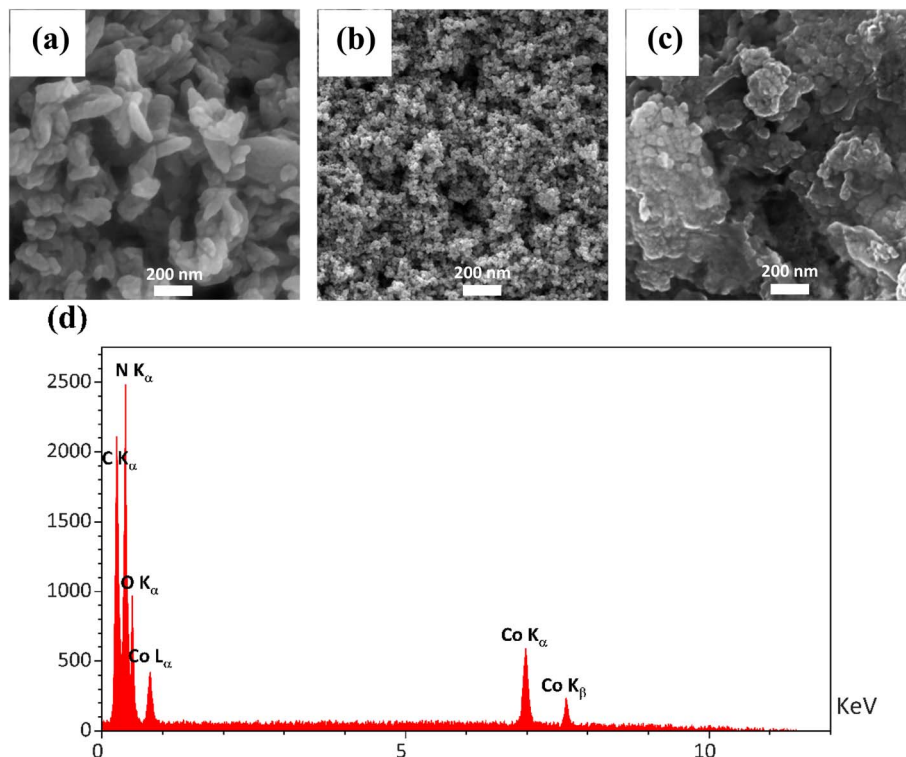


Fig. 3 FESEM image of (a) g-C<sub>3</sub>N<sub>4</sub> nanoplates, (b) LiCoO<sub>2</sub> nanoparticles, and (c) GL3 hybrid materials. (d) EDX spectra of GL3 sample.

verifies that the g-C<sub>3</sub>N<sub>4</sub>@LiCoO<sub>2</sub> nanocomposite contains components like Co, O, C, and N.

The morphology of the as-synthesized g-C<sub>3</sub>N<sub>4</sub>, LiCoO<sub>2</sub> nanoparticle and g-C<sub>3</sub>N<sub>4</sub>/LiCoO<sub>2</sub> nanocomposites were characterized by TEM. Fig. 4a clearly illustrated that the as-obtained g-C<sub>3</sub>N<sub>4</sub> samples are nanosheets. Fig. 4b clearly illustrates small spherical structure of LiCoO<sub>2</sub> nanoparticles. Fig. 4c show LiCoO<sub>2</sub> nanoparticles with average size of ~25 nm, anchored on the g-C<sub>3</sub>N<sub>4</sub> nanosheet are evident.

XPS analysis investigated the elemental composition and valence states in the g-C<sub>3</sub>N<sub>4</sub>@LiCoO<sub>2</sub> nanocomposites. The XPS spectrum in Fig. 5a confirms the presence of Li, Co, O, N, and C elements in the nanocomposites without any impurities. In Fig. 5b, the Co 2p spectrum displays a Co 2p<sub>3/2</sub> main peak at 778.1 eV with a satellite peak at 786.5 eV, along with a Co 2p<sub>1/2</sub>

main peak at 794.6 eV with a satellite peak at 800.1 eV. The ratio of Co 2p<sub>3/2</sub> to Co 2p<sub>1/2</sub> is approximately 2/1, indicating the presence of Co<sup>3+</sup> atoms in the synthesized products.<sup>45–48</sup> The peak of Li 1s photoelectrons observed at a binding energy of 55.4 eV confirms the presence of Li (Fig. 5c).<sup>49</sup> Additionally, Fig. 5d illustrates distinct peaks in the GL3 composite at 284.7 eV for C–C bonds and 288.1 eV for N=C–N bonds. The N 1s spectrum in Fig. 5e reveals peak positions for carbon, nitrogen, and hydrogen (C–N–H) bonds at 401.2 eV and C–N=C bonds at 398.9 eV.<sup>50</sup> The characterization data for the GL<sub>3</sub> electrocatalyst confirm the successful synthesis of the nanocomposite using a straightforward method.

The results obtained from BET measurements are depicted in Fig. 6. The pure g-C<sub>3</sub>N<sub>4</sub> and GL3 nanocomposites exhibit significant hysteresis in the relative pressure range of 0 < P/P<sub>0</sub> <

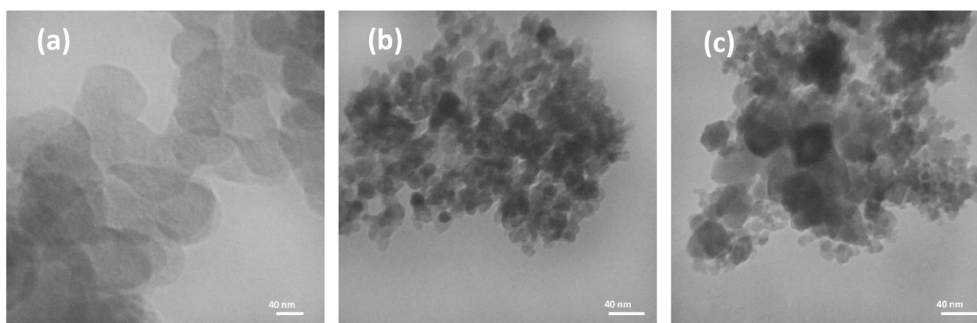


Fig. 4 TEM image of (a) g-C<sub>3</sub>N<sub>4</sub> nanoplates, (b) LiCoO<sub>2</sub> nanoparticles, and (c) GL3 hybrid materials.



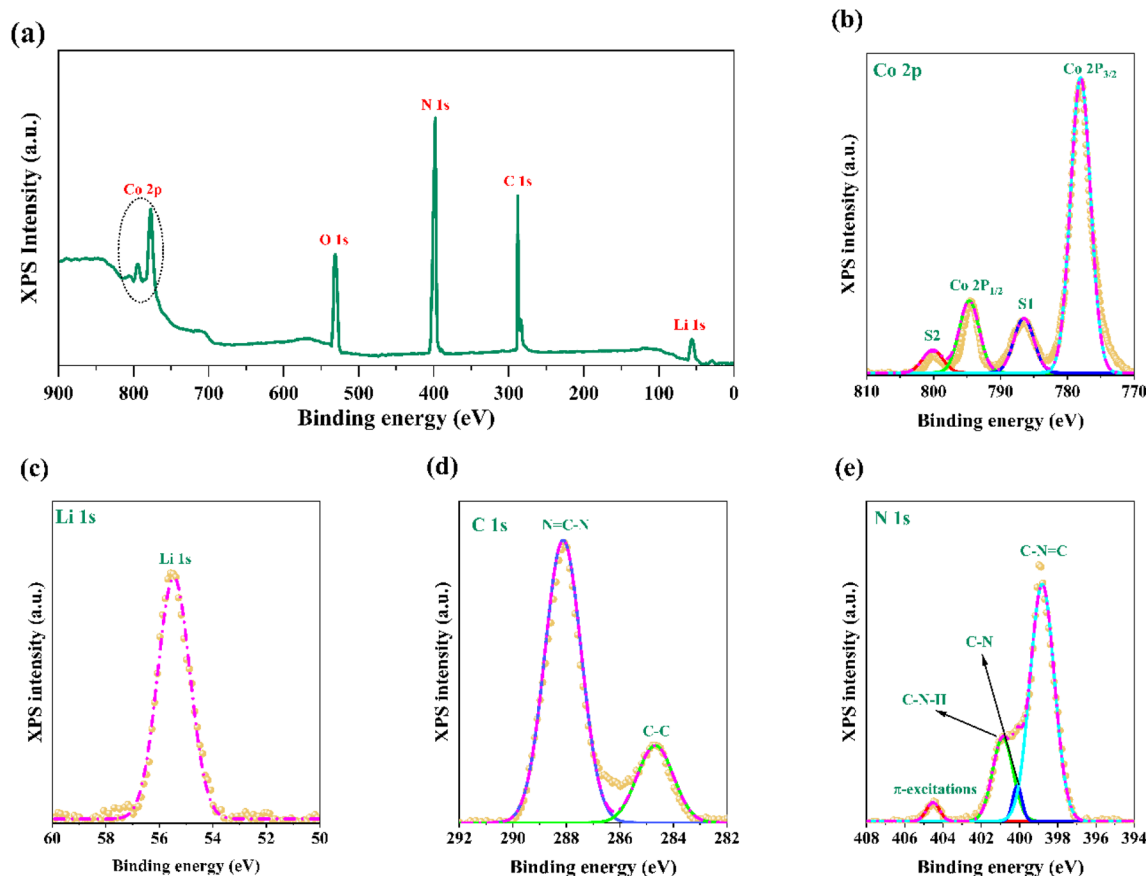


Fig. 5 (a) XPS spectra of GL3 sample. High-resolution XPS for (b) Co 2p, (c) Li 1s, (d) C 1s, and (e) N 1s elements.

1, as shown in Fig. 6a and b. Compared to the pure g-C<sub>3</sub>N<sub>4</sub> with a surface area of 15.81 m<sup>2</sup> g<sup>-1</sup> and average pore size of 11.649 nm, the GL3 nanocomposites have a higher specific surface area of 23.74 m<sup>2</sup> g<sup>-1</sup> and average pore size of 8.727 nm. This increase could be advantageous for concentrating target substances in subsequent electrochemical sensing applications.<sup>51</sup>

The electrochemical performance of g-C<sub>3</sub>N<sub>4</sub>@LiCoO<sub>2</sub> nanocomposites was evaluated using cyclic voltammetry (CV) and

electrochemical impedance spectroscopy (EIS). Fig. 7a and b depict CV curves obtained at a scan rate of 50 mV s<sup>-1</sup>. All measurements were performed in a 0.1 M KNO<sub>3</sub> solution containing 2 mM K<sub>3</sub>[Fe(CN)<sub>6</sub>]. The CV curve for g-C<sub>3</sub>N<sub>4</sub>/GCE exhibited small, approximately symmetrical redox peaks at 294 mV and 67 mV, representing the anodic (*E*<sub>pa</sub>) and cathodic (*E*<sub>pc</sub>) peaks, respectively. The CV curve for GL3/GCE displayed a more prominent pair of redox peaks, with *E*<sub>pa</sub> at 366 mV and *E*<sub>pc</sub> at 279 mV. This suggests that incorporating LiCoO<sub>2</sub> into the

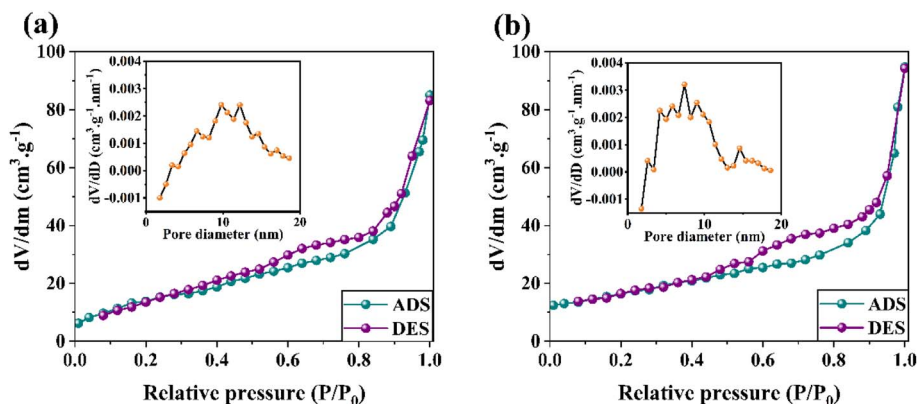


Fig. 6 N<sub>2</sub> adsorption-desorption response and BJH pore size distributions of (a) g-C<sub>3</sub>N<sub>4</sub> and (b) GL3 samples.

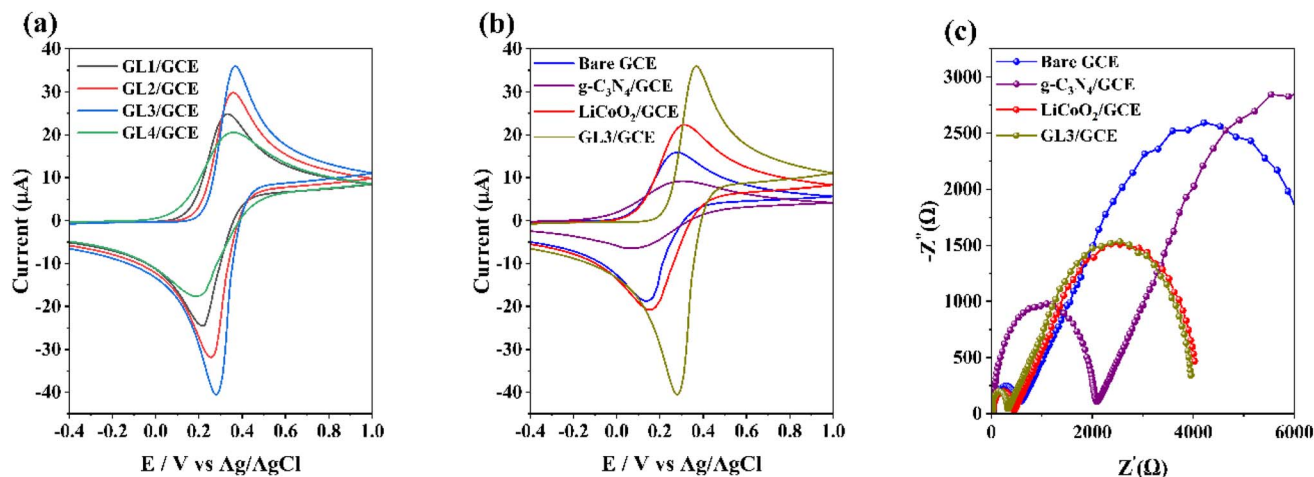


Fig. 7 (a) CV curves of different  $g\text{-C}_3\text{N}_4\text{@LiCoO}_2/\text{GCEs}$  at scan rate  $50 \text{ mV s}^{-1}$ : GL1, GL2, GL3, and GL4. (b) CV curves of bare GCE,  $g\text{-C}_3\text{N}_4/\text{GCE}$ ,  $\text{LiCoO}_2/\text{GCE}$ , and  $g\text{-C}_3\text{N}_4\text{@LiCoO}_2/\text{GCE}$  (GL3/GCE) at scan rate  $50 \text{ mV s}^{-1}$ . All tests were conducted for  $2 \text{ mM K}_3[\text{Fe}(\text{CN})_6]$  in  $0.1 \text{ M KNO}_3$  solution. (c) Nyquist plot of EIS for bare GCE,  $g\text{-C}_3\text{N}_4/\text{GCE}$ ,  $\text{LiCoO}_2/\text{GCE}$ , and  $g\text{-C}_3\text{N}_4\text{@LiCoO}_2/\text{GCE}$  (GL3/GCE).

$g\text{-C}_3\text{N}_4/\text{GCE}$  enhanced the electrochemical activity. Compared to  $\text{LiCoO}_2/\text{GCE}$  and  $g\text{-C}_3\text{N}_4/\text{GCE}$ , the GL3/GCE exhibited a more negative oxidation potential and significantly higher peak currents. This indicates that the  $\text{LiCoO}_2$  component improved the electron transfer kinetics and increased the electroactive surface area. The peak currents of GL3/GCE gradually increased with increasing amounts of  $\text{LiCoO}_2$ , suggesting that the  $\text{LiCoO}_2$  component played a crucial role in enhancing the electrochemical activity. However, excessive  $\text{LiCoO}_2$  doping in GL4/GCE slightly decreased the peak currents, possibly due to the shielding of active sites on the  $g\text{-C}_3\text{N}_4$  surface. Overall, GL3/GCE demonstrated the highest charge transfer efficiency and the best electrochemical activity among all the investigated electrodes. This makes it a promising candidate for sensing applications. Incorporating  $\text{LiCoO}_2$  into the  $g\text{-C}_3\text{N}_4/\text{GCE}$  composite significantly enhanced its electrochemical properties. The optimized GL3/GCE exhibited superior charge transfer kinetics and electrocatalytic activity, making it a promising material for sensing applications.

The Nyquist plot provides insights into the interfacial charge transfer kinetics and the resistance of the electrode–electrolyte interface. The Nyquist impedance graphs for  $\text{LiCoO}_2/\text{GCE}$ ,  $g\text{-C}_3\text{N}_4\text{@LiCoO}_2/\text{GCE}$  (GL3/GCE), and  $g\text{-C}_3\text{N}_4/\text{GCE}$  are displayed in Fig. 7c. A reduced arc radius signifies enhanced charge migration efficiency across the electrode–electrolyte interface, with the electron-transfer resistance behavior on the electrode surface being mirrored by the arc radius at elevated frequencies.<sup>32,52</sup> The Nyquist plot of the GCE revealed a confined

semicircular region, as illustrated in Fig. 7c, indicating minimal electron transfer resistance on its surface. The arc radius grew following  $g\text{-C}_3\text{N}_4$  coating, suggesting  $g\text{-C}_3\text{N}_4$  inhibited electron transfer. The arc radius of the resulting GL3/GCE demonstrated a noticeable, progressive decrease if the  $g\text{-C}_3\text{N}_4/\text{LiCoO}_2$  nano-composites were coated, suggesting that the  $\text{LiCoO}_2$  can reduce the interfacial resistance. The charge transfer resistances for the bare-GCE,  $g\text{-C}_3\text{N}_4/\text{GCE}$ ,  $\text{LiCoO}_2/\text{GCE}$ , and  $g\text{-C}_3\text{N}_4\text{@LiCoO}_2/\text{GCE}$  are measured at  $487.3 \Omega$ ,  $1984.5 \Omega$ ,  $398.7 \Omega$ , and  $264.6 \Omega$ , respectively.

Table 1 presents electrochemical parameters for various electrode materials tested in a  $2 \text{ mM K}_3[\text{Fe}(\text{CN})_6]$  solution with  $0.1 \text{ M KNO}_3$  at a scan rate of  $50 \text{ mV s}^{-1}$ . The study compares bare GCE,  $g\text{-C}_3\text{N}_4/\text{GCE}$ ,  $\text{LiCoO}_2/\text{GCE}$ , and  $g\text{-C}_3\text{N}_4\text{@LiCoO}_2/\text{GCE}$  electrodes. The  $g\text{-C}_3\text{N}_4\text{@LiCoO}_2/\text{GCE}$  electrode demonstrates superior electrochemical performance across all measured parameters. It exhibits the highest anodic ( $I_{\text{pa}}$ ) and cathodic ( $I_{\text{pc}}$ ) peak currents, indicating enhanced electron transfer capabilities. Additionally, this electrode shows the lowest potential difference ( $\Delta E$ ) between anodic and cathodic peaks, suggesting improved reversibility of the electrochemical process. The performance of the electrodes can be ranked as follows:

$$g\text{-C}_3\text{N}_4\text{@LiCoO}_2/\text{GCE} > \text{LiCoO}_2/\text{GCE} > \text{bare GCE} > g\text{-C}_3\text{N}_4/\text{GCE}$$

The  $g\text{-C}_3\text{N}_4/\text{GCE}$  performs poorly with the lowest peak currents and highest  $\Delta E$ , indicating slower electron transfer

Table 1 Electrochemical parameters of different samples were recorded at a scan rate of  $50 \text{ mV s}^{-1}$  for  $2 \text{ mM K}_3[\text{Fe}(\text{CN})_6]$  containing  $0.1 \text{ M KNO}_3$

Sample	$E_{\text{pa}}$ (mV)	$E_{\text{pc}}$ (mV)	$I_{\text{pa}}$ ( $\mu\text{A}$ )	$I_{\text{pc}}$ ( $\mu\text{A}$ )	$I_{\text{pa}}/I_{\text{pc}}$	$\Delta E$ (mV)
Bare GCE	271	142	15.93	−18.81	0.847	129
$g\text{-C}_3\text{N}_4/\text{GCE}$	294	67	9.19	−6.42	1.431	227
$\text{LiCoO}_2/\text{GCE}$	305	163	22.36	−20.72	0.926	142
$g\text{-C}_3\text{N}_4\text{@LiCoO}_2/\text{GCE}$	366	279	35.55	−40.38	0.828	87

kinetics and lower reversibility. The GCE and LiCoO<sub>2</sub>/GCE electrodes demonstrate intermediate performance, with LiCoO<sub>2</sub>/GCE generally outperforming g-C<sub>3</sub>N<sub>4</sub>/GCE. The outstanding performance of g-C<sub>3</sub>N<sub>4</sub>@LiCoO<sub>2</sub>/GCE suggests a synergistic effect between g-C<sub>3</sub>N<sub>4</sub> and LiCoO<sub>2</sub> when combined. This synergy improves electrochemical properties compared to the individual components or the bare electrode. The enhanced electron transfer kinetics, and stable electrochemical process make g-C<sub>3</sub>N<sub>4</sub>@LiCoO<sub>2</sub>/GCE a promising electrode material for potential applications in electrochemical sensing or energy storage devices. This analysis highlights the importance of composite materials in enhancing electrochemical performance and demonstrates the potential of g-C<sub>3</sub>N<sub>4</sub>@LiCoO<sub>2</sub> as an advanced electrode material for various electrochemical applications.

Fig. 8a graph shows CV curves of g-C<sub>3</sub>N<sub>4</sub>@LiCoO<sub>2</sub>/GCE in PBS (pH 7) containing 10 nM malathion at different scan rates ranging from 10 to 200 mV s<sup>-1</sup>. The x-axis represents the potential (*E*) in volts vs. Ag/AgCl, ranging from -0.4 to 1.0 V. By conducting CV measurements with various scan rates ranging from 10 to 200 mV s<sup>-1</sup>, the kinetic and transport characteristics of the malathion molecules on the g-C<sub>3</sub>N<sub>4</sub>@LiCoO<sub>2</sub>/GCE were further characterized (Fig. 8a). The CV curves show increasing peak currents with higher scan rates, indicating a surface-controlled electrochemical process for malathion on g-C<sub>3</sub>N<sub>4</sub>@LiCoO<sub>2</sub>/GCE. Regression correlations between *I*<sub>pa</sub> and *I*<sub>pc</sub> and the square of scan rate *v* are as follows:

$$I_{pa} = 3.544v^{1/2} - 4.466 \quad (R^2 = 0.968) \text{ and}$$

$$I_{pc} = -1.708v^{1/2} - 1.245 \quad (R^2 = 0.857).$$

The Fig. 8b suggests a surface-controlled mechanism for malathion on g-C<sub>3</sub>N<sub>4</sub>@LiCoO<sub>2</sub>/GCE, rather than a diffusion-controlled process.<sup>53</sup> Table 2 presents electrochemical parameters (*E*<sub>pa</sub>, *E*<sub>pc</sub>, *I*<sub>pa</sub>, *I*<sub>pc</sub>, *I*<sub>pa</sub>/*I*<sub>pc</sub> ratio, and  $\Delta E$ ) at various scan rates, supporting the conclusion that surface adsorption primarily governs the electrochemical behavior of malathion on the modified electrode.

**Table 2** Electrochemical parameters of g-C<sub>3</sub>N<sub>4</sub>@LiCoO<sub>2</sub>/GCE (GL3) evaluated from the CV in PBS (pH 7) with 10 nM malathion

Scan rate (mV s <sup>-1</sup> )	<i>E</i> <sub>pa</sub> (mV)	<i>E</i> <sub>pc</sub> (mV)	<i>I</i> <sub>pa</sub> (μA)	<i>I</i> <sub>pc</sub> (μA)	<i>I</i> <sub>pa</sub> / <i>I</i> <sub>pc</sub>	$\Delta E$ (mV)
10	364	203	4.57	-3.74	1.222	161
25	357	254	11.41	-8.52	1.339	103
50	410	341	23.76	-16.79	1.415	69
75	437	349	29.24	-18.26	1.601	88
100	458	354	32.24	-20.48	1.574	104
125	478	365	34.11	-20.32	1.679	113
150	498	362	38.73	-21.10	1.836	136
200	519	353	43.47	-22.83	1.904	166

The DPV method, with a potential window of -0.400 to +0.800 V, a scan rate of 50 mV s<sup>-1</sup>, and a sensitivity of  $1.0 \times 10^{-5}$  A V<sup>-1</sup>, was employed to investigate the impact of malathion concentration further using C<sub>3</sub>N<sub>4</sub>@LiCoO<sub>2</sub>/GCE in 0.1 M PBS under optimized conditions (Fig. 9a). The oxidation peak current at approximately 0.4 V is directly proportional to the malathion concentration. Within a range of malathion concentrations (CMA) from 5 to 120 nM, the current response on g-C<sub>3</sub>N<sub>4</sub>@LiCoO<sub>2</sub>/GCE increased linearly with rising CMA. A linear regression analysis on the collected data resulted in the equation  $I = 1.632\text{conc.} + 5.949$ , where *I* (μA) represents the current response, showing a high correlation coefficient of  $R^2 = 0.99439$  (Fig. 9b).

Fig. 10a displays the stability test results for DPV response signals over 16 days. The graph shows a gradual decrease in current from an initial value of 49.32 μA at day 0 to 39.91 μA at day 16. This test was conducted in a 0.1 M PBS solution (pH 7) containing 30 nM of malathion. The decreasing trend suggests a slight degradation in sensor performance over time. However, the sensor retains about 81% of its initial response after 16 days, indicating relatively good stability for the tested period. The minimal detectable concentration was determined using the formula  $\text{LOD} = 3\sigma/m$ . From the results, the standard deviation ( $\sigma$ ) derived from 6 measurements was calculated to be

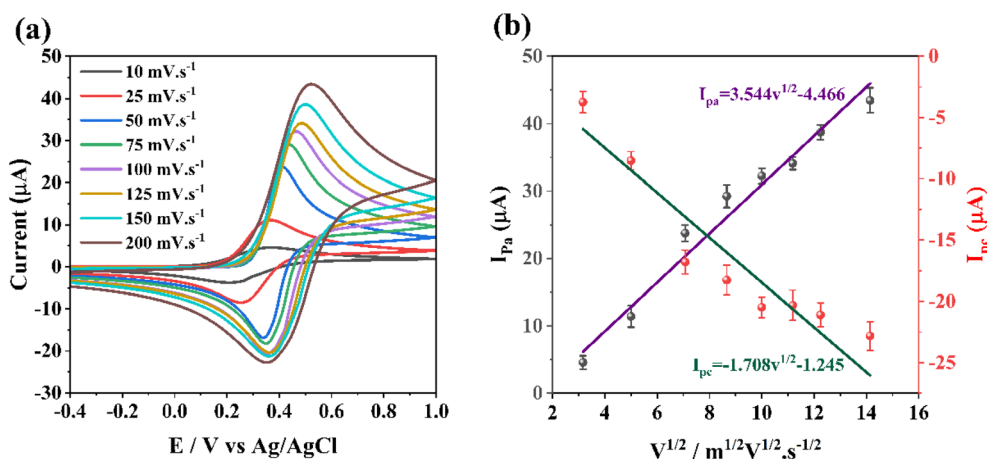


**Fig. 8** (a) CV curves of g-C<sub>3</sub>N<sub>4</sub>@LiCoO<sub>2</sub>/GCE in PBS (pH 7) containing 10 nM malathion at various scan rates. (b) The curves of anodic and cathodic peak currents regarding the square of scan rate.



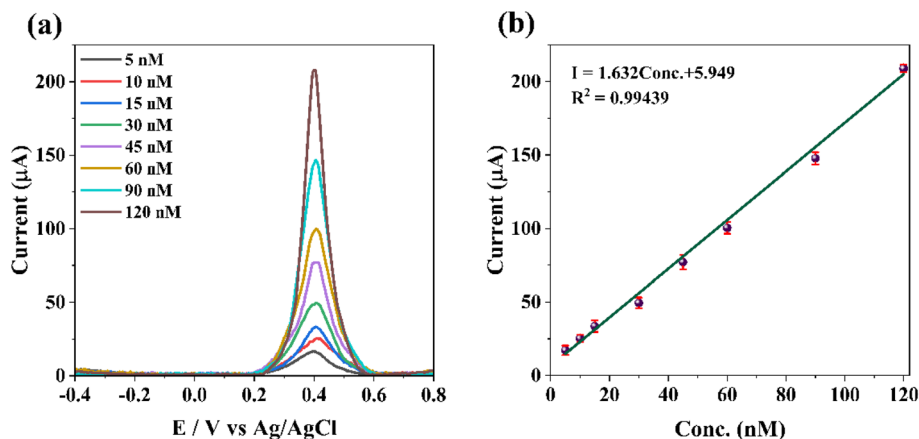


Fig. 9 (a) DPV plots for different concentrations (5–120 nM) of malathion based on the g-C<sub>3</sub>N<sub>4</sub>@LiCoO<sub>2</sub>/GCE electrode at pH 7 (0.1 M PBS solution). (b) The calibration curve of DPSV current at the g-C<sub>3</sub>N<sub>4</sub>@LiCoO<sub>2</sub>/GCE electrode versus malathion concentration.

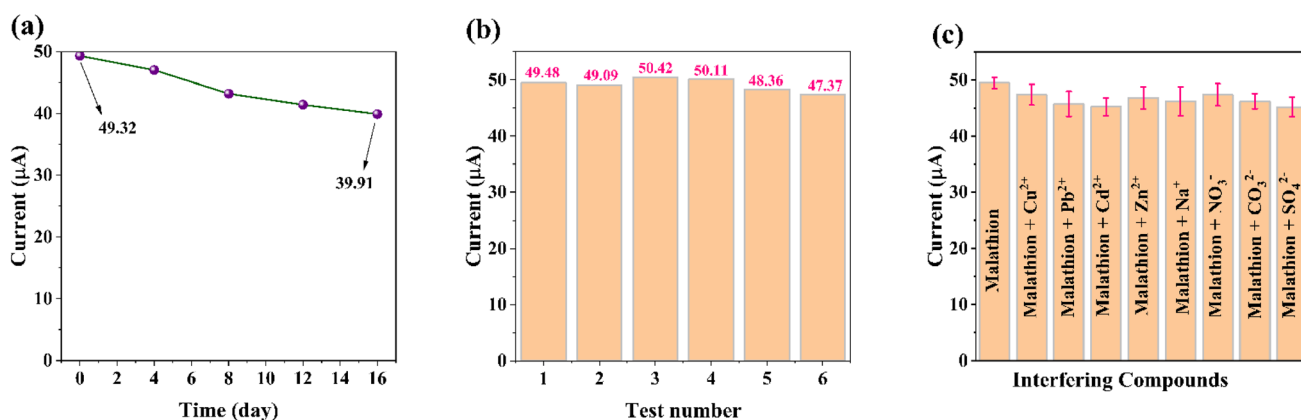


Fig. 10 (a) DPV response signals for stability test along 16 days in 0.1 M PBS (pH 7) solution in the presence of 30 nM of malathion. (b) Reproducibility of g-C<sub>3</sub>N<sub>4</sub>@LiCoO<sub>2</sub>/GCE towards malathion during 6 individual tests in the presence of 30 nM of malathion (in 0.1 M PBS (pH 7) solution). (c) DPV peak current of g-C<sub>3</sub>N<sub>4</sub>@LiCoO<sub>2</sub>/GCE sensor for malathion detection (30 nM) in the presence of 300  $\mu M$  of different interferences.  $1.632x + 5.949$ .

1.14 nM (Fig. 10b). In comparison, the slope ( $m$ ) of the calibration curve was measured at 1.632 (Fig. 9b). Consequently, the modified electrode's minimal detection limit (LOD) within the linear range was established as 2.096 nM.<sup>54,55</sup>

Fig. 10c depicts the DPV peak current density of g-C<sub>3</sub>N<sub>4</sub>@LiCoO<sub>2</sub>/GCE sensor for detecting of malathion in the presence of various interfering compounds, such as Cu<sup>2+</sup>, Pb<sup>2+</sup>, Cd<sup>2+</sup>, Zn<sup>2+</sup>, Na<sup>+</sup>, NO<sub>3</sub><sup>-</sup>, CO<sub>3</sub><sup>2-</sup>, and SO<sub>4</sub><sup>2-</sup>. The observed trend in Fig. 10c reveal that the g-C<sub>3</sub>N<sub>4</sub>@LiCoO<sub>2</sub>/GCE sensor with an anti-interfering response is suitable for the selective detection of malathion.

Table 3 shows the measured amount of malathion based on the g-C<sub>3</sub>N<sub>4</sub>@LiCoO<sub>2</sub>/GCE sensor. As listed in Table 3, the recovery range of the designed sensor for different malathion concentrations is 96.76% to 98.64%. This indicates that the electrochemical g-C<sub>3</sub>N<sub>4</sub>@LiCoO<sub>2</sub>/GCE sensor can be used as a potential candidate for practical applications to detect malathion.

Table 4 illustrates the performance of the g-C<sub>3</sub>N<sub>4</sub>@LiCoO<sub>2</sub>/GCE sensor was compared with that of other previously

Table 3 Recovery studies of spiked malathion in lettuce samples for g-C<sub>3</sub>N<sub>4</sub>@LiCoO<sub>2</sub>/GCE electrode

Sample	Spike (nM)	$I_{pa}$ ( $\mu A$ )	Found ( $\mu M$ )	Recovery (%)
Lettuce	00	Not found	Not found	Not found
	40	69.51	38.95	97.37
	40	69.43	38.90	97.24
	40	69.25	38.79	96.98
	80	133.22	77.98	97.48
	80	132.87	77.77	97.21
	80	134.73	78.91	98.64
	120	198.81	118.17	98.47
	120	196.38	116.69	97.24
	120	195.44	116.11	96.76

reported modified electrodes for the electrochemical measurement of malathion. Comparable to other electrodes developed by other authors, the developed electrode shown good limit of detection and linear range.



Table 4 Comparison of sensing parameters for the electrochemical detection of malathion using different electrode materials

Electrodes	Techniques	LOD	Linear range	References
CdS/g-C <sub>3</sub> N <sub>4</sub> /Sm-BDC/GCE	DPV	$7.4 \times 10^{-9}$ M	$3.0\text{--}15.0 \times 10^{-8}$ M	56
GQDs/GCE	DPV	0.62 nM	1 to 30 $\mu$ M	57
CuO/NiO/PANI	DPV	$2 \times 10^{-6}$ mol L <sup>-1</sup>	20–2500 mol L <sup>-1</sup>	58
Cu <sup>2+</sup> -g-C <sub>3</sub> N <sub>4</sub>	OP	6.798 nM	70–800 nM	59
COF@MWCNT/ACH	DPV	0.5 $\mu$ M	0.001–10.0 $\mu$ M	60
g-C <sub>3</sub> N <sub>4</sub> @LiCoO <sub>2</sub> /GCE	DPV	4.38 nM	5–120 nM	This work

## 4. Conclusion

Consequently, the development of a promising electrochemical probe for malathion detection based on green g-C<sub>3</sub>N<sub>4</sub>@LiCoO<sub>2</sub> nanocomposites represents a significant advancement in pesticide detection and environmental monitoring. The g-C<sub>3</sub>N<sub>4</sub>@LiCoO<sub>2</sub> nanostructures with appropriate LiCoO<sub>2</sub> doping can significantly enhance the electrocatalytic activity of g-C<sub>3</sub>N<sub>4</sub>. This improvement in electrocatalytic activity can be attributed to increased electrical conductivity, enhanced electron transfer, and an increased number of active sites on the electrode surface. Therefore, g-C<sub>3</sub>N<sub>4</sub>@LiCoO<sub>2</sub> nanostructures can serve as promising electrocatalytic materials for various electrochemical applications. This innovative sensor design offers a cost-effective and sensitive solution sensor with an acceptable recovery range for malathion probing and aligns with the growing demand for sustainable agricultural practices.

## Data availability

The data that support the findings of this study are available from the corresponding author upon reasonable request.

## Author contributions

All authors contributed equally in this paper.

## Conflicts of interest

The authors declare that they have no conflict of interest.

## Acknowledgements

The authors extend their appreciation to the Deanship of Scientific Research at King Khalid University for funding this work through the large group Research Project under grant number RGP 2/315/45.

## References

- 1 E. Serag, A. El-Maghraby, N. Hassan and A. El Nemr, CuO@MWCNTs nanocomposite as non-enzyme electrochemical sensor for the detection of malathion in seawater, *Desalin. Water Treat.*, 2021, **236**, 240–249.
- 2 Y. Xie, Y. Yu, L. Lu, X. Ma, L. Gong, X. Huang, G. Liu and Y. Yu, CuO nanoparticles decorated 3D graphene nanocomposite as non-enzymatic electrochemical sensing platform for malathion detection, *J. Electroanal. Chem.*, 2018, **812**, 82–89.
- 3 V. Philippe, A. Neveen, A. Marwa and A.-Y. A. Basel, Occurrence of pesticide residues in fruits and vegetables for the Eastern Mediterranean Region and potential impact on public health, *Food Control*, 2021, **119**, 107457.
- 4 N. Kaur, H. Thakur and N. Prabhakar, Multi walled carbon nanotubes embedded conducting polymer based electrochemical aptasensor for estimation of malathion, *Microchem. J.*, 2019, **147**, 393–402.
- 5 J. A. Buledi, N. Mahar, A. Mallah, A. R. Solangi, I. M. Palabiyik, N. Qambrani, F. Karimi, Y. Vasseghian and H. Karimi-Maleh, Electrochemical quantification of mancozeb through tungsten oxide/reduced graphene oxide nanocomposite: a potential method for environmental remediation, *Food Chem. Toxicol.*, 2022, **161**, 112843.
- 6 C. Tejada-Casado, D. Moreno-González, F. J. Lara, A. M. García-Campaña and M. del Olmo-Iruela, Determination of benzimidazoles in meat samples by capillary zone electrophoresis tandem mass spectrometry following dispersive liquid–liquid microextraction, *J. Chromatogr. A*, 2017, **1490**, 212–219.
- 7 D. Harshit, K. Charmy and P. Nrupesh, Organophosphorus pesticides determination by novel HPLC and spectrophotometric method, *Food Chem.*, 2017, **230**, 448–453.
- 8 T. Zhou, X. Xiao and G. Li, Microwave accelerated selective Soxhlet extraction for the determination of organophosphorus and carbamate pesticides in ginseng with gas chromatography/mass spectrometry, *Anal. Chem.*, 2012, **84**, 5816–5822.
- 9 N. K. Mogha, V. Sahu, M. Sharma, R. K. Sharma and D. T. Masram, Biocompatible ZrO<sub>2</sub>-reduced graphene oxide immobilized AChE biosensor for chlorpyrifos detection, *Mater. Des.*, 2016, **111**, 312–320.
- 10 Y. Yang, X. Liu, M. Wu, X. Wang, T. Hou and F. Li, Electrochemical biosensing strategy for highly sensitive pesticide assay based on mercury ion-mediated DNA conformational switch coupled with signal amplification by hybridization chain reaction, *Sens. Actuators, B*, 2016, **236**, 597–604.
- 11 A. Hulanicki, S. Glab and F. Ingman, Chemical sensors: definitions and classification, *Pure Appl. Chem.*, 1991, **63**, 1247–1250.
- 12 P. S. Miri, N. Khosroshahi, M. Darabi Goudarzi and V. Safarifard, MOF-biomolecule nanocomposites for electrosensing, *Nanochem. Res.*, 2021, **6**, 213–222.



- 13 N. P. Shetti, D. S. Nayak, K. R. Reddy and T. M. Aminabhavi, Graphene–clay-based hybrid nanostructures for electrochemical sensors and biosensors, *Graphene-based Electrochemical Sensors for Biomolecules*, Elsevier, 2019, pp. 235–274.
- 14 H. Karimi-Maleh, M. Ghalkhani, Z. S. Dehkordi, J. Singh, Y. Wen, M. Baghayeri, J. Rouhi, L. Fu and S. Rajendran, MOF-enabled pesticides as developing approach for sustainable agriculture and reducing environmental hazards, *J. Ind. Eng. Chem.*, 2024, **129**, 105–123.
- 15 H. Teymourinia, S. Rtimi, M. Ghalkhani, A. Ramazani and T. M. Aminabhavi, Flower-like nanocomposite of carbon quantum dots, MoS<sub>2</sub>, and dendritic Ag-based Z-scheme type photocatalysts for effective tartrazine degradation, *Chem. Eng. J.*, 2023, **473**, 145239.
- 16 M. Saleh Mohammadnia, H. Roghani-Mamaqani, M. Ghalkhani and S. Hemmati, A modified electrochemical sensor based on N,S-doped carbon dots/carbon nanotube-poly(amidoamine) dendrimer hybrids for imatinib mesylate determination, *Biosensors*, 2023, **13**, 547.
- 17 M. Ghalkhani, H. Teymourinia, F. Ebrahimi, N. Irannejad, H. Karimi-Maleh, C. Karaman, F. Karimi, E. N. Dragoi, E. Lichtfouse and J. Singh, Engineering and application of polysaccharides and proteins-based nanobiocatalysts in the recovery of toxic metals, phosphorous, and ammonia from wastewater: a review, *Int. J. Biol. Macromol.*, 2023, **242**, 124585.
- 18 Z. Liu, J. Tao, Z. Zhu, Y. Zhang, H. Wang, P. Pang, H. Wang and W. Yang, A sensitive electrochemical assay for T4 polynucleotide kinase activity based on Fe<sub>3</sub>O<sub>4</sub>@TiO<sub>2</sub> and gold nanoparticles hybrid probe modified magnetic electrode, *J. Electrochem. Soc.*, 2022, **169**, 027504.
- 19 X. Zhu, H. Zheng, X. Wei, Z. Lin, L. Guo, B. Qiu and G. Chen, Metal–organic framework (MOF): a novel sensing platform for biomolecules, *Chem. Commun.*, 2013, **49**, 1276–1278.
- 20 G. He, L. Tian, Y. Cai, S. Wu, Y. Su, H. Yan, W. Pu, J. Zhang and L. Li, Sensitive nonenzymatic electrochemical glucose detection based on hollow porous NiO, *Nanoscale Res. Lett.*, 2018, **13**, 1–10.
- 21 J. Tang, X. Ma, J. Yang, D.-D. Feng and X.-Q. Wang, Recent advances in metal–organic frameworks for pesticide detection and adsorption, *Dalton Trans.*, 2020, **49**, 14361–14372.
- 22 Y. Dai and X. Kan, From non-electroactive to electroactive species: highly selective and sensitive detection based on a dual-template molecularly imprinted polymer electrochemical sensor, *Chem. Commun.*, 2017, **53**, 11755–11758.
- 23 V. N. Palakollu, D. Chen, J.-N. Tang, L. Wang and C. Liu, Recent advancements in metal–organic frameworks composites based electrochemical (bio) sensors, *Microchim. Acta*, 2022, **189**, 161.
- 24 M. Thakur, B. Wang and M. L. Verma, Development and applications of nanobiosensors for sustainable agricultural and food industries: recent developments, challenges and perspectives, *Environ. Technol. Innovation*, 2022, **26**, 102371.
- 25 S. Nikhar and P. Kumar, Electrochemical sensing of malathion using doped MOFs, *IOP Conference Series: Materials Science and Engineering*, IOP Publishing, 2022, p. 012055.
- 26 R. Prasad, A. Bhattacharyya and Q. D. Nguyen, Nanotechnology in sustainable agriculture: recent developments, challenges, and perspectives, *Front. Microbiol.*, 2017, **8**, 1014.
- 27 T. Talaviya, D. Shah, N. Patel, H. Yagnik and M. Shah, Implementation of artificial intelligence in agriculture for optimisation of irrigation and application of pesticides and herbicides, *Artif. Intell. Agric.*, 2020, **4**, 58–73.
- 28 M. Ghalkhani, M. H. Khaneghah and E. Sohouli, Graphitic carbon nitride: synthesis and characterization, *Handbook of Carbon-Based Nanomaterials*, Elsevier, 2021, pp. 573–590.
- 29 M. Ghalkhani, N. Irannejad, E. Sohouli, R. Keçili and C. M. Hussain, Environmental applications of nanographitic carbon nitride, *Nanoremediation*, Elsevier, 2023, pp. 187–227.
- 30 H.-B. Wang, H.-D. Zhang, L.-L. Xu, T. Gan, K.-J. Huang and Y.-M. Liu, Electrochemical biosensor for simultaneous determination of guanine and adenine based on dopamine-melanin colloidal nanospheres–graphene composites, *J. Solid State Electrochem.*, 2014, **18**, 2435–2442.
- 31 A. Kumar, J. Makasana, M. Rekha, R. Sharma, A. F. Al-Hussainy, M. Agarwal, S. Saini, M. Dehghanipour and M. K. Abosoda, Design and synthesis of new active LiCoO<sub>2</sub>/rGO nanocomposites for electrochemical hydrogen storage application, *Mater. Chem. Phys.*, 2024, 130318.
- 32 Z. Mao, J. Chen, Y. Yang, D. Wang, L. Bie and B. D. Fahlman, Novel g-C<sub>3</sub>N<sub>4</sub>/CoO nanocomposites with significantly enhanced visible-light photocatalytic activity for H<sub>2</sub> evolution, *ACS Appl. Mater. Interfaces*, 2017, **9**, 12427–12435.
- 33 W. Che, W. Cheng, T. Yao, F. Tang, W. Liu, H. Su, Y. Huang, Q. Liu, J. Liu and F. Hu, Fast photoelectron transfer in (C<sub>ring</sub>)-C<sub>3</sub>N<sub>4</sub> plane heterostructural nanosheets for overall water splitting, *J. Am. Chem. Soc.*, 2017, **139**, 3021–3026.
- 34 G. Zhang, Z.-A. Lan, L. Lin, S. Lin and X. Wang, Overall water splitting by Pt/g-C<sub>3</sub>N<sub>4</sub> photocatalysts without using sacrificial agents, *Chem. Sci.*, 2016, **7**, 3062–3066.
- 35 W.-J. Ong, L.-L. Tan, Y. H. Ng, S.-T. Yong and S.-P. Chai, Graphitic carbon nitride (g-C<sub>3</sub>N<sub>4</sub>)-based photocatalysts for artificial photosynthesis and environmental remediation: are we a step closer to achieving sustainability?, *Chem. Rev.*, 2016, **116**, 7159–7329.
- 36 Y. Zhang, T. Mori, L. Niu and J. Ye, Non-covalent doping of graphitic carbon nitride polymer with graphene: controlled electronic structure and enhanced optoelectronic conversion, *Energy Environ. Sci.*, 2011, **4**, 4517–4521.
- 37 M. Tiwari, A. Singh, D. Thakur and S. K. Pattanayek, Graphitic carbon nitride-based concoction for detection of melamine and R6G using surface-enhanced Raman scattering, *Carbon*, 2022, **197**, 311–323.
- 38 S. Morang, A. Bandyopadhyay, N. Borah, A. Kar, B. B. Mandal and N. Karak, Photoluminescent Self-Healable Waterborne Polyurethane/Mo and S Codoped Graphitic Carbon Nitride



- Nanocomposite with Bioimaging and Encryption Capability, *ACS Appl. Bio Mater.*, 2024, 7, 1910–1924.
- 39 W. Chang, W. Xue, E. Liu, J. Fan and B. Zhao, Highly efficient H<sub>2</sub> production over NiCo<sub>2</sub>O<sub>4</sub> decorated g-C<sub>3</sub>N<sub>4</sub> by photocatalytic water reduction, *Chem. Eng. J.*, 2019, **362**, 392–401.
  - 40 Y. Liu, X. Li, H. He, S. Yang, G. Jia and S. Liu, CoP imbedded g-C<sub>3</sub>N<sub>4</sub> heterojunctions for highly efficient photo, electro and photoelectrochemical water splitting, *J. Colloid Interface Sci.*, 2021, **599**, 23–33.
  - 41 N. Wu, Y. Zhang, Y. Guo, S. Liu, H. Liu and H. Wu, Flake like LiCoO<sub>2</sub> with exposed {010} facets as a stable cathode material for highly reversible lithium storage, *ACS Appl. Mater. Interfaces*, 2016, **8**, 2723–2731.
  - 42 K. Tan, M. Reddy, G. S. Rao and B. Chowdari, High-performance LiCoO<sub>2</sub> by molten salt (LiNO<sub>3</sub>: LiCl) synthesis for Li-ion batteries, *J. Power Sources*, 2005, **147**, 241–248.
  - 43 C. Julien, Local cationic environment in lithium nickel-cobalt oxides used as cathode materials for lithium batteries, *Solid State Ionics*, 2000, **136**, 887–896.
  - 44 M. Haripriya, T. Manimekala, G. Dharmalingam, M. Minakshi and R. Sivasubramanian, Asymmetric supercapacitors based on ZnCo<sub>2</sub>O<sub>4</sub> nanohexagons and orange peel derived activated carbon electrodes, *Chem.-Asian J.*, 2024, **19**, e202400202.
  - 45 L. Dahéron, H. Martinez, R. Dedryvère, I. Baraille, M. Ménétrier, C. Denage, C. Delmas and D. Gonbeau, Surface properties of LiCoO<sub>2</sub> investigated by XPS analyses and theoretical calculations, *J. Phys. Chem. C*, 2009, **113**, 5843–5852.
  - 46 L. Liu, H. Zhang, J. Yang, Y. Mu and Y. Wang, Fabrication of Fe-Doped LiCoO<sub>2</sub> Sandwich-Like Nanocomposites as Excellent Performance Cathode Materials for Lithium-Ion Batteries, *Chem.-Eur. J.*, 2015, **21**, 19104–19111.
  - 47 Y. Liu, W. Gao, J. Zhan, Y. Bao, R. Cao, H. Zhou and L. Liu, One-pot synthesis of Ag-H<sub>3</sub>PW<sub>12</sub>O<sub>40</sub>-LiCoO<sub>2</sub> composites for thermal oxidation of airborne benzene, *Chem. Eng. J.*, 2019, **375**, 121956.
  - 48 L. Dahéron, R. Dedryvère, H. Martinez, M. Ménétrier, C. Denage, C. Delmas and D. Gonbeau, Electron transfer mechanisms upon lithium deintercalation from LiCoO<sub>2</sub> to CoO<sub>2</sub> investigated by XPS, *Chem. Mater.*, 2008, **20**, 583–590.
  - 49 R. Dedryvère, D. Foix, S. Franger, S. Patoux, L. Daniel and D. Gonbeau, Electrode/electrolyte interface reactivity in high-voltage spinel LiMn<sub>1.6</sub>Ni<sub>0.4</sub>O<sub>4</sub>/Li<sub>4</sub>Ti<sub>5</sub>O<sub>12</sub> lithium-ion battery, *J. Phys. Chem. C*, 2010, **114**, 10999–11008.
  - 50 P. Chaudhary and P. P. Ingole, *In Situ* solid-state synthesis of 2D/2D interface between Ni/NiO hexagonal nanosheets supported on g-C<sub>3</sub>N<sub>4</sub> for enhanced photo-electrochemical water splitting, *Int. J. Hydrogen Energy*, 2020, **45**, 16060–16070.
  - 51 N. M. Hussein, T. J. Al-Musawi, N. Kumar, R. Sharma, A. I. Mohammed, I. Sharma, T. Kalyani, M. Dehghanipour and A. Sandhu, The first and cost-effective nanobiocomposite ZnPor/rGO/TiO<sub>2</sub> as efficient UV photocatalysts for ethylparaben decomposition, *Inorg. Chem. Commun.*, 2024, **170**, 113541.
  - 52 M. Y. Emran, A. Kotb, A. B. Ganganboina, A. Okamoto, T. Z. Abolibda, H. A. Alzahrani, S. M. Gomha, C. Ma, M. Zhou and M. A. Shenashen, Tailored portable electrochemical sensor for dopamine detection in human fluids using heteroatom-doped three-dimensional g-C<sub>3</sub>N<sub>4</sub> hornet nest structure, *Anal. Chim. Acta*, 2024, **1320**, 342985.
  - 53 B. Su, Y. Chen, X. Yang, J. Han, H. Jia, P. Jing and Y. Wang, Amperometric sensor based on carbon nanotubes and polycations for the determination of vitamin C, *Int. J. Electrochem. Sci.*, 2017, **12**, 6417–6427.
  - 54 M. Naseri, L. Fotouhi and A. Ehsani, Nanostructured Metal–Organic Framework Modified Glassy Carbon Electrode as a High Efficient Non-Enzymatic Amperometric Sensor for Electrochemical Detection of H<sub>2</sub>O<sub>2</sub>, *J. Electrochem. Sci. Technol.*, 2018, **9**, 28–36.
  - 55 N. Gao, R. Tan, Z. Cai, H. Zhao, G. Chang and Y. He, A novel electrochemical sensor via Zr-based metal–organic framework–graphene for pesticide detection, *J. Mater. Sci.*, 2021, **56**, 19060–19074.
  - 56 J. M. Yassin, A. M. Taddesse, A. A. Tsegaye and M. Sánchez-Sánchez, CdS/g-C<sub>3</sub>N<sub>4</sub>/Sm-BDC MOF nanocomposite modified glassy carbon electrodes as a highly sensitive electrochemical sensor for malathion, *Appl. Surf. Sci.*, 2024, **648**, 158973.
  - 57 S. Tanwar, A. Sharma and D. Mathur, A graphene quantum dots–glassy carbon electrode-based electrochemical sensor for monitoring malathion, *Beilstein J. Nanotechnol.*, 2023, **14**, 701–710.
  - 58 K. Ghanbari and Z. Babaei, Fabrication and characterization of non-enzymatic glucose sensor based on ternary NiO/CuO/polyaniline nanocomposite, *Anal. Biochem.*, 2016, **498**, 37–46.
  - 59 Y. Chen, Y. Zhu, Y. Zhao and J. Wang, Fluorescent and colorimetric dual-response sensor based on copper (II)-decorated graphitic carbon nitride nanosheets for detection of toxic organophosphorus, *Food Chem.*, 2021, **345**, 128560.
  - 60 X. Wang, S. Yang, J. Shan and X. Bai, Novel electrochemical acetylcholinesterase biosensor based on core-shell covalent organic framework@multi-walled carbon nanotubes (COF@MWCNTs) composite for detection of malathion, *Int. J. Electrochem. Sci.*, 2022, **17**, 220543.

